The Company of Biologists

RESEARCH ARTICLE

Planar cell polarity-dependent asymmetric organization of microtubules for polarized positioning of the basal body in node cells

Xiaorei Sai[1,§§], Yayoi Ikawa[1,2], Hiromi Nishimura[1,2], Katsutoshi Mizuno[1,*], Eriko Kajikawa[1], Takanobu A. Katoh[1], Toshiya Kimura[1,‡,§], Hidetaka Shiratori[2,¶], Katsuyoshi Takaoka[2,**], Hiroshi Hamada[1,2,§§] and Katsura Minegishi[1,2,‡‡]

ABSTRACT

For left-right symmetry breaking in the mouse embryo, the basal body must become positioned at the posterior side of node cells, but the precise mechanism for this has remained unknown. Here, we examined the role of microtubules (MTs) and actomyosin in this basal body positioning. Exposure of mouse embryos to agents that stabilize or destabilize MTs or F-actin impaired such positioning. Active myosin II was detected at the anterior side of node cells before the posterior shift of the basal body, and this asymmetric activation was lost in Prickle and dachsous mutant embryos. The organization of basal-body associated MTs (baMTs) was asymmetric between the anterior and posterior sides of node cells, with anterior baMTs extending horizontally and posterior baMTs extending vertically. This asymmetry became evident after polarization of the PCP core protein Vangl1 and before the posterior positioning of the basal body, and it also required the PCP core proteins Prickle and dachsous. Our results suggest that the asymmetry in baMT organization may play a role in correct positioning of the basal body for left-right symmetry breaking.

KEY WORDS: Basal body, Cilia, Left-right asymmetry, Planar cell polarity, Mouse

INTRODUCTION

In fish, amphibians and mammals, breaking of left-right (L-R) symmetry is mediated by unidirectional fluid flow at the L-R organizer of the embryo (Blum et al., 2014). In the mouse embryo, leftward fluid flow at the ventral node (the L-R organizer of the mouse embryo) is generated by clockwise rotational movement of motile cilia of pit cells located in the central region of the node (Nonaka et al., 1998). The rotational axis of these motile cilia is not vertical but is instead tilted toward the posterior side of the embryo (Nonaka et al., 2005; Okada et al., 2005), which allows the clockwise rotation of the cilia to give rise to the leftward fluid flow. The tilt of the motile cilium of each pit cell correlates with the position of the corresponding basal body within the cell (Hashimoto et al., 2010). The rotational axis is thus almost vertical when the basal body is located at the center of the cell during early development (early headfold stage), whereas it is tilted toward the posterior side of the embryo when the basal body later becomes positioned at the posterior side of a pit cell (three-somite stage).

The positioning of the basal body in pit cells is under the control of planar cell polarity (PCP), the coordinated alignment of cell polarity across a tissue plane (Devenport, 2016; Goodrich and Strutt, 2011; Wallingford and Mitchell, 2011). Pit cells are polarized along the anterior-posterior (A-P) axis as a result of their sensing the graded distribution of Wnt5 activity (Minegishi et al., 2017). PCP core proteins such as Vangl1 and Prickle (Pk) thus become localized to the anterior side of pit cells, whereas Dvl becomes localized to the posterior side (Antic et al., 2010; Hashimoto et al., 2010; Song et al., 2010). Such polarized localization of PCP core proteins is required for correct positioning of the basal body in node pit cells and for consequent generation of the unidirectional nodal flow (Antic et al., 2010; Hashimoto et al., 2010; Minegishi et al., 2017; Song et al., 2010).

Although the genetic pathway responsible for regulation of the position of the basal body in pit cells has been largely characterized, how this position actually changes from the central to the posterior region of the cell has remained unknown. We have now examined the role of microtubules (MTs) and actomyosin in translocation of the basal body in pit cells, and have thereby clarified the hierarchical relation among PCP core proteins, MTs and actomyosin. Our results suggest that asymmetric organization of basal body-associated microtubules (baMTs) contributes to basal body positioning by providing force.

RESULTS

Dachsous plays a permissive role in node cell polarization for establishment of L-R asymmetry

Dachsous functions as a PCP core protein in *Drosophila*. Vertebrates possess two dachsous genes, *Dchs1* and *Dchs2*. Whereas *Dchs1* mutant mice manifest defects in mammary glands (Mao et al., 2011), vertebrae (Crespo-Enriquez et al., 2019; Mao et al., 2016) and the mitral valve (Durst et al., 2015), the role of *Dchs2* in mouse development has remained unknown. To examine

DEVELOPMENT

the role of dachsous genes in establishment of A-P polarity at the node of mouse embryos, we generated double-mutant mice lacking both *Dchs1* and *Dchs2* (Fig. S1A,B).

Dchs2$^{-/-}$ and *Dchs1*$^{+/-}$;*Dchs2*$^{-/-}$ mice did not manifest obvious defects. Mating of *Dchs1*$^{+/-}$;*Dchs2*$^{-/-}$ mice with each other revealed that *Dchs1*$^{-/-}$;*Dchs2*$^{-/-}$ mice were born at a frequency of 19.79% (19/96 mice), which is slightly lower than the expected 25%, suggesting that a portion of the *Dchs1*$^{-/-}$;*Dchs2*$^{-/-}$ animals died during embryogenesis. Moreover, all *Dchs1*$^{-/-}$;*Dchs2*$^{-/-}$ mice died within 24 h after birth.

The mutant embryos were examined for Vangl1 localization in pit cells of the node. Whereas Vangl1 was localized at the apical membrane at the anterior side of pit cells in *Dchs1*$^{+/-}$;*Dchs2*$^{-/-}$ embryos at the two- to four-somite stage, this A-P distribution was disrupted in *Dchs1*$^{-/-}$;*Dchs2*$^{-/-}$ embryos (Fig. 1A). Vangl1 was thus localized at the apical membrane without A-P polarity in *Dchs1*$^{-/-}$; *Dchs2*$^{-/-}$ embryos, and it was also found in the cytoplasm either at a low level (11/17 embryos) or a high level (6/17 embryos) in these embryos (Fig. 1A-C). Anteriorly polarized localization of Vangl2 was similarly disrupted in *Dchs1*$^{-/-}$;*Dchs2*$^{-/-}$ embryos (Fig. S2). Furthermore, the basal body of pit cells failed to become positioned posteriorly in the absence of Dchs1 and Dchs2. Thus, whereas most basal bodies were located at the posterior region of pit cells in *Dchs1*$^{+/-}$;*Dchs2*$^{+/-}$ embryos, with an average basal body position (ABP) of 0.327, those of *Dchs1*$^{-/-}$;*Dchs2*$^{-/-}$ embryos failed to show a posterior localization, with an ABP of 0.190 (Fig. 2). Indeed, the leftward nodal flow that was apparent in *Dchs1*$^{+/-}$;*Dchs2*$^{+/-}$ embryos (Fig. 1D) was impaired in most (7/11) of the *Dchs1*$^{-/-}$; *Dchs2*$^{-/-}$ embryos examined (Fig. 1E). Finally, left-sided *Nodal* expression in the lateral plate mesoderm was lost (4/9) or downregulated (3/9) in *Dchs1*$^{-/-}$;*Dchs2*$^{-/-}$ embryos, whereas Nodal expression at the node was maintained (Fig. 1F).

Dachsous manifests a polarized localization in wing cells of *Drosophila*. We therefore examined the subcellular localization of
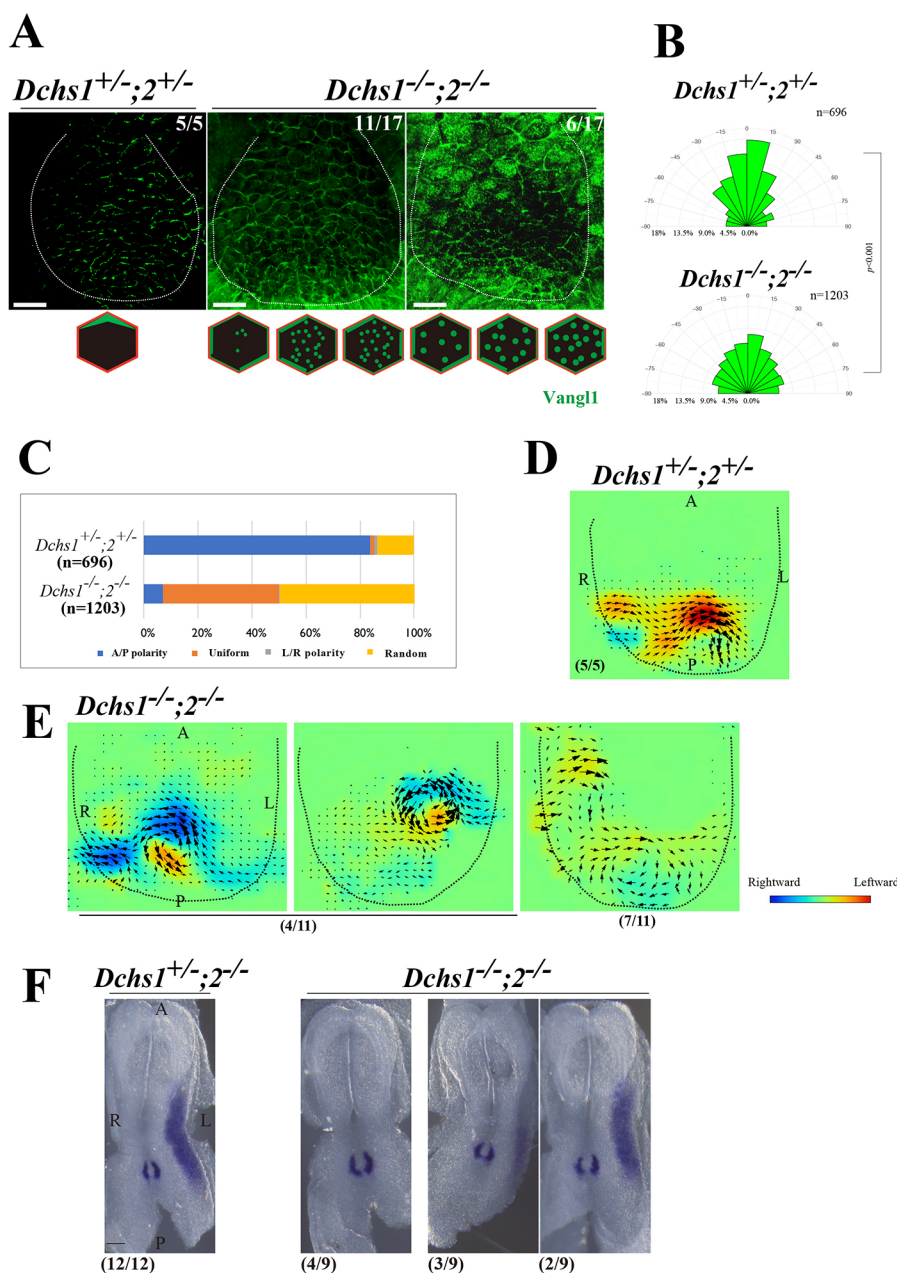

Fig. 1. Polarized localization of Vangl1 and nodal flow are dependent on dachsous genes. (A) Immunofluorescence localization of Vangl1 in node cells of *Dchs1*$^{+/-}$;*Dchs2*$^{+/-}$ (control) and *Dchs1*$^{-/-}$;*Dchs2*$^{-/-}$ mouse embryos at the two- to four-somite stage. The white dashed lines indicate the outline of the node. The L-R and A-P axes are indicated, as are the numbers of embryos examined showing each phenotype. The localization of Vangl1 in node cells is also shown schematically below the corresponding images. The polarized distribution of Vangl1 is impaired in *Dchs1*$^{-/-}$;*Dchs2*$^{-/-}$ embryos. (B) Quantitative analysis of the Vangl1 localization pattern in node cells of individual embryos of the indicated genotypes. The angle (–90° to +90°) in the rose diagrams was determined by quantitative analysis for each cell and is shown categorized into 12 classes (15° for each class). The length of each bar indicates the cell number for each class. The number of cells analyzed was 696 from five *Dchs1*$^{+/-}$;*Dchs2*$^{+/-}$ embryos and 1203 from 17 *Dchs1*$^{-/-}$;*Dchs2*$^{-/-}$ embryos. The *P*-value was determined with the Mardia-Watson-Wheeler test. (C) Frequency of various patterns of Vangl1 localization in *Dchs1*$^{+/-}$;*Dchs2*$^{+/-}$ and *Dchs1*$^{-/-}$; *Dchs2*$^{-/-}$ embryos. (D,E) Nodal flow in *Dchs1*$^{+/-}$; *Dchs2*$^{+/-}$ (D) and *Dchs1*$^{-/-}$;*Dchs2*$^{-/-}$ (E) embryos at the two- to five-somite stage was examined by PIV analysis with fluorescent microbeads. The black dashed line indicates the outline of the node. Small arrows indicate the direction and velocity of the flow at the indicated positions. The relative color scale indicates the magnitude of the flow velocity (leftward in red, rightward in blue). Leftward flow was detected in control embryos (D), whereas the direction of the flow was randomized (4/11 embryos) or the flow was almost lost (7/11 embryos) in *Dchs1*$^{-/-}$;*Dchs2*$^{-/-}$ embryos (E). (F) Embryos with the indicated genotype were examined for *Nodal* expression at the three-somite stage. Note that *Nodal* expression in the lateral plate, which was left-sided in *Dchs1*$^{+/-}$; *Dchs2*$^{-/-}$ embryos (12/12 embryos), was lost (4/9 embryos), downregulated (3/9 embryos) or maintained (2/9 embryos) in *Dchs1*$^{-/-}$;*Dchs2*$^{-/-}$ embryos. *Nodal* expression at the node was maintained in all cases. A, anterior; L, left; P, posterior; R, right. Scale bars: 10 µm (A); 200 mm (F).
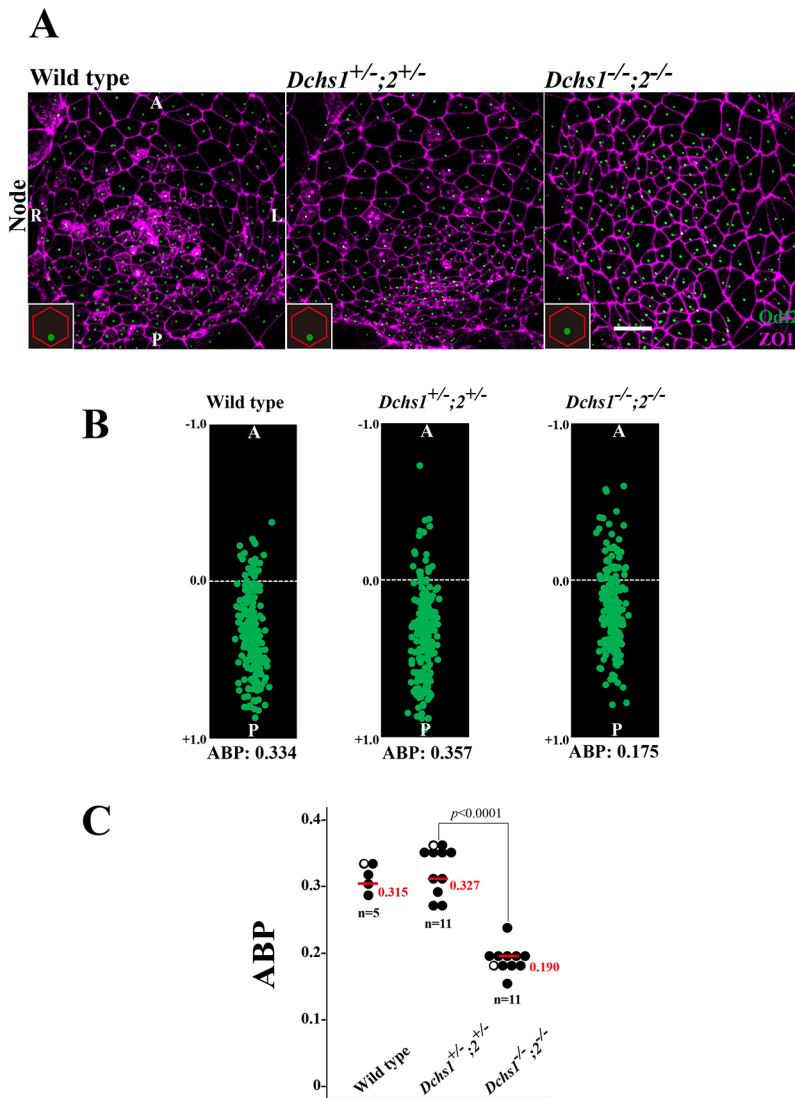
Fig. 2. Dachsous is required for correct positioning of the basal body in node cells. (A) Mouse embryos of the indicated genotypes at the three- to four-somite stage were subjected to immunofluorescence staining of the tight junction protein ZO1 (magenta) and the basal body protein Odf2 (green). The L-R and A-P axes are indicated, and the position of the basal body in node cells is shown schematically in the insets. (B) The relative position of the basal body in node cells of individual embryos of the indicated genotypes at the three- to four-somite stage was determined as in A. Each green dot corresponds to a single node cell. The ABP of each embryo is shown. (C) Summary of ABP values for embryos of the indicated genotypes. Each point denotes the ABP of a single embryo, with the red bars indicating mean values. The P-value was determined with Tukey's honest significance test. Scale bar: 10 µm.

Dchs1 in node pit cells with the use of specific antibodies (Tsukasaki et al., 2014). In $Dchs1^{+/-};Dchs2^{+/-}$ embryos, Dchs1 was detected at the apical and lateral cell membrane, without A-P polarity, whereas Dchs1 signals were absent in pit cells of $Dchs1^{-/-};Dchs2^{-/-}$ embryos (Fig. 3A). Given that specific antibodies to Dchs2 were not available, we generated a $Dchs2^{Venus/+}$ mouse strain, in which the coding sequence for the fluorescent protein Venus is fused in frame to that for the COOH-terminus of Dchs2 (Fig. S1C). Similar to Dchs1, the Dchs2::Venus protein was detected in node pit cells, being found mostly at the cell membrane without obvious A-P polarity (Fig. 3B). These results suggested that dachsous plays a permissive role in polarization of node pit cells along the A-P axis, which is essential for the generation of unidirectional fluid flow at the node (Antic et al., 2010; Hashimoto et al., 2010; Song et al., 2010).

Microtubules and actomyosin are required both to shift and to maintain the position of the basal body in node cells

The cytoskeleton contributes to the establishment of PCP in the epidermis of *Drosophila* and in various organs of vertebrates (Devenport, 2014; Harumoto et al., 2010). We examined the possible role of MTs and actomyosin in positioning of the basal body in node pit cells with the use of various pharmacological agents that affect the mass or dynamics of the cytoskeleton. Mouse embryos at the late headfold stage, when the basal body is not positioned at the posterior side of pit cells (Hashimoto et al., 2010), were incubated with the various agents until they achieved the three-somite stage (Fig. 4A). In wild-type (WT) embryos incubated with dimethyl sulfoxide (DMSO) vehicle, the basal body was shifted to the posterior side of pit cells, with an ABP of 0.307. Nocodazole at a concentration that destabilizes MTs (30 µM) prevented this shift in basal body position. Taxol (paclitaxel), which stabilizes MTs, and a lower concentration of nocodazole that does not destabilize MTs but affects MT dynamics (100 nM) (Liao et al., 1995) also each inhibited the posterior shift of the basal body, suggesting that the proper dynamics of MTs is required for basal body positioning. Jasplakinolide, which stabilizes filamentous (F-) actin, as well as ML-7 and blebbistatin, which inhibit myosin II activity, all similarly blocked the posterior localization of the basal body, implicating actomyosin in basal body positioning. ciliobrevin D, an inhibitor of dynein motors, showed no inhibitory effect in this assay. These results thus suggested that not only the presence of MTs and actomyosin but also their proper dynamics are essential for the posterior positioning of the basal body in pit cells.

We found that MTs and actomyosin are also required to maintain the position of the basal body after it has translocated to the posterior

side of pit cells. Incubation of embryos at the three-somite stage (when the basal body has been positioned at the posterior side) with various agents until they achieved the five-somite stage thus revealed that nocodazole, blebbistatin, ML-7 and jasplakinolide each induced a shift in the position of the basal body back to a central location (Fig. 4B).

Functional cross talk between MTs and actomyosin is mediated by various mechanisms (Dogterom and Koenderink, 2019). Indeed, we found that the formation of MTs and that of F-actin in node cells are interdependent. Destabilization of MTs with nocodazole was thus associated with the pattern of cortical F-actin becoming wavy as well as with a reduction in the amount of cytoplasmic F-actin (Fig. S3). Conversely, inhibition of actin polymerization with latrunculin A was associated with shrinkage of the aster of baMTs (Fig. S4).

Myosin II is activated at the anterior side of node cells via Rac1

Our results suggested that actomyosin may contribute to translocation of the basal body in pit cells by providing mechanical force. We next examined whether nonmuscle myosin II is activated in pit cells using immunofluorescence staining with antibodies specific for a phosphorylated form of myosin light chain (pMLC). We observed weak pMLC signals in pit cells of WT embryos at the late bud (LB) stage (Fig. 5A), and pMLC was detected uniformly at the early headfold stage (Fig. 5B), before the basal body has changed its position (Hashimoto et al., 2010). The localization of pMLC began to

show A-P polarity at the one-somite stage (Fig. 5C), when a subtle posterior shift of the basal body is also apparent (Hashimoto et al., 2010). At the two- to three-somite stage, when the posterior positioning of the basal body is almost complete, pMLC signals clearly manifested A-P polarization, being localized to the anterior side of the cell (Fig. 5D). This A-P polarity was confirmed by examination of sagittal sections of the node, which revealed pMLC to be localized at the cell cortex on the anterior side of pit cells (Fig. 5E). In all, the A-P polarity and intensity of pMLC signals increase from the LB stage to the three-somite stage (Fig. 5F,G).

The A-P polarization of active myosin II was impaired in $Dchs1^{-/-}$; $Dchs2^{-/-}$, $Pk1$ (also known as $Prickle1$)$^{-/-}$;$Pk2$ ($Prickle2$)$^{-/-}$ and $Sfrp1^{-/-}$;$Sfrp2^{-/-}$;$Sfrp5^{-/-}$ mutant embryos (Fig. 6A-D). Active myosin II staining at the apical membrane was thus attenuated and had lost A-P polarity in $Dchs1^{-/-}$;$Dchs2^{-/-}$ and $Pk1^{-/-}$;$Pk2^{-/-}$ embryos at the two- to three-somite stage. Active myosin II was detected at a higher level in the embryos lacking the three Sfrp proteins (which serve as endogenous Wnt inhibitors) than in the other mutant embryos, but it had also lost its A-P polarization. These results suggested that nonmuscle myosin II is activated at the anterior side of pit cells at the time of basal body translocation, and that this activation occurs downstream of Sfrp/Wnt5 and PCP core proteins.

Activation of nonmuscle myosin II is mediated by several mechanisms, one of which is dependent on Rac1 (Pasapera et al., 2015; Shibata et al., 2015). We found that posterior translocation of the basal body in node pit cells was inhibited by the Rac1 inhibitor NSC23766 (Fig. S5), consistent with previous observations
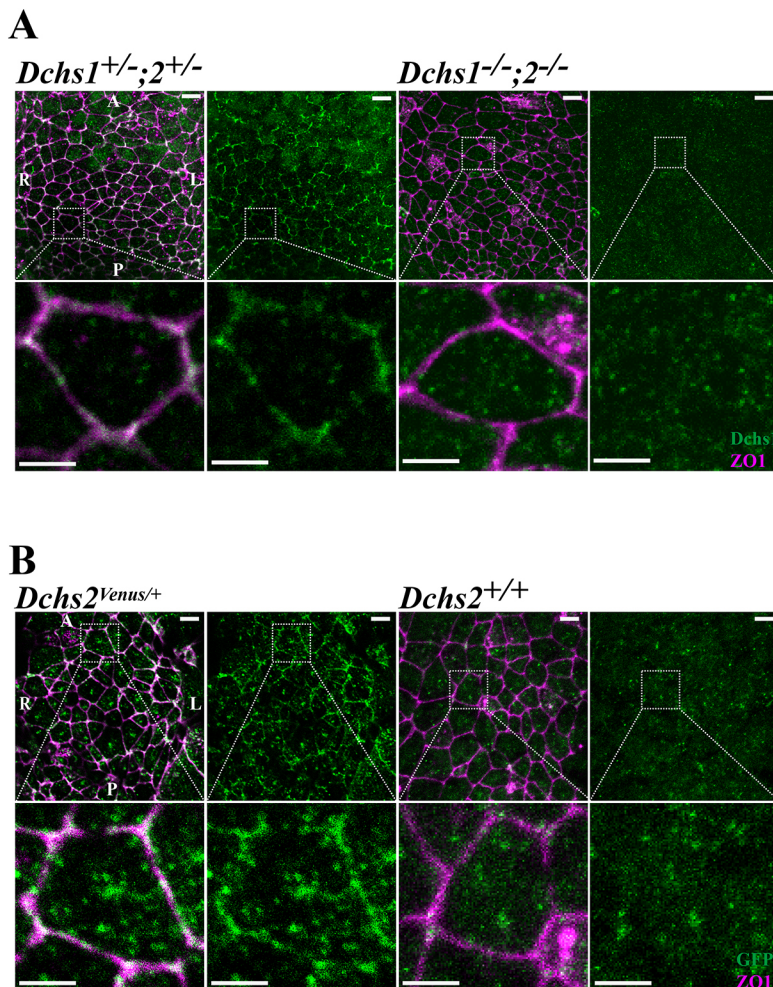

Fig. 3. Subcellular localization of Dchs1 and Dchs2 in node cells. (A) Immunofluorescence analysis of Dchs1 (green) and ZO1 (magenta) in the node region of $Dchs1^{+/-}$;$Dchs2^{+/-}$ and $Dchs1^{-/-}$; $Dchs2^{-/-}$ embryos at embryonic day (E) 7.5. The boxed regions in the upper panels are shown at higher magnification in the lower panels. Dchs1 is uniformly located at the cell membrane and is present at a low level in the cytosolic compartment of $Dchs1^{+/-}$; $Dchs2^{+/-}$ embryos. The L-R and A-P axes are indicated. (B) Immunofluorescence staining of the node with antibodies to ZO1 (magenta) and with those to green fluorescence protein (GFP, green) for detection of Venus in $Dchs2^{Venus/+}$ and $Dchs2^{+/+}$ embryos at E7.5. The boxed regions in the upper panels are shown at higher magnification in the lower panels. The Dchs2::Venus protein was uniformly localized at the membrane of $Dchs2^{Venus/+}$ embryos. Scale bars: 5 μm.
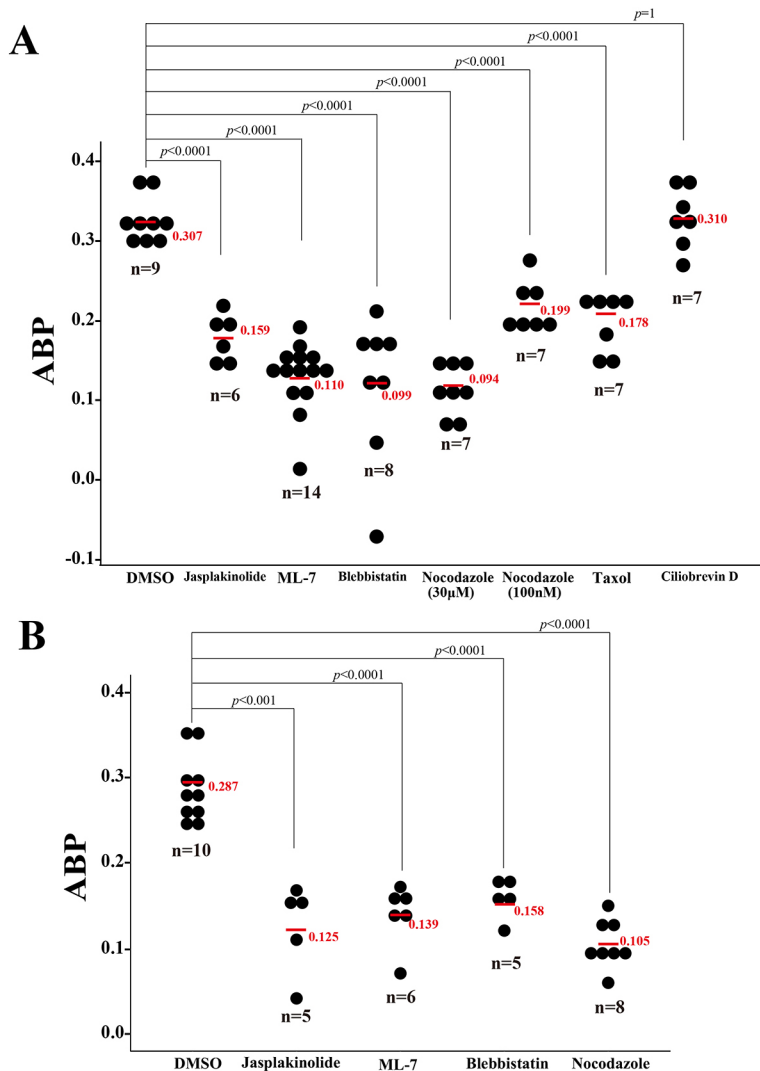
Fig. 4. Effects of various cytoskeleton-targeted agents on basal body positioning in pit cells of mouse embryos. (A) Summary of ABP values for WT embryos that had been cultured with DMSO vehicle, jasplakinolide (3 µM), ML-7 (25 µM), blebbistatin (25 µM), nocodazole (30 µM or 100 nM), Taxol (5 µM) or ciliobrevin D (40 µM) from the late headfold stage to the three-somite stage. The overall morphology of the cultured embryos remained normal. Each dot denotes the ABP of a single embryo, with the red bars indicating mean values. The P-values were determined with Dunnett's test. (B) Summary of ABP values for embryos that had been cultured with DMSO, jasplakinolide (3 µM), ML-7 (25 µM), blebbistatin (25 µM) or nocodazole (30 µM) from the three-somite stage to the five-somite stage.

(Hashimoto et al., 2010), but that it was not inhibited by the Rho kinase (ROCK) inhibitor Y-27632 (Fig. S5), suggesting that Rac1 may contribute to basal body translocation by activating myosin II. Indeed, the GTP-bound (active) form of Rac1 was detected at the apical side of node pit cells (Fig. S6A,B), and GTP-Rac1 signals were attenuated by treatment of embryos with NSC23766 (Fig. S6C). GTP-Rac1 was detected at the zero-somite as well as the three-somite stage (Fig. S6A,B), consistent with the appearance of pMLC on the anterior side of node cells (Fig. 5C,D). Furthermore, incubation of embryos from the late bud stage to the three-somite stage in the presence of NSC23766 abolished pMLC signals in pit cells (Fig. 6E,F). These results suggested that myosin II is activated in node pit cells via Rac1. Inhibition of pMLC by ML-7 or inhibition of Rac1 by NSC23766 did not disrupt anteriorly polarized localization of Vangl1 (Fig. 7), suggesting that Vangl1 polarization is upstream of the Rac1-mediated activation of myosin II. However, nocodazole impaired the polarized localization of Vangl1 and reduced the level of Vangl1 at the cell cortex (Fig. 7), suggesting that MTs play multiple roles in basal body positioning.

PCP core proteins regulate basal body-associated astral microtubules

We next examined baMTs in node pit cells. In ventral views, an array of microtubules was seen to extend from the basal body at the

apical side of node cells of WT embryos at the early headfold and three-somite stages (Fig. 8A), when the basal body remains at the center of the cell. At the three-somite stage, when the basal body has shifted toward the posterior side of node cells, an organized array of MT fibers was apparent, extending from the basal body to the cell cortex (Fig. 8A). This organized pattern of MTs was disrupted in $Pk1^{-/-};Pk2^{-/-}$ and $Dchs1^{-/-};Dchs2^{-/-}$ embryos, with ventral views of both mutants showing that most baMTs at the apical side of pit cells were connected to the basal body but did not extend linearly, instead appearing wavy (Fig. 8B,C). Treatment of WT embryos with ML-7 resulted in shortening of baMTs (Fig. 8D). These results thus implicated PCP core proteins in the regulation of baMTs.

Organization of MTs is A-P asymmetric before the shift in basal body position

To observe the distribution pattern of MTs along the apicobasal axis, we prepared sagittal sections of the node at various stages including the late bud, early headfold and three-somite stages, and those that contained the basal body were selected (Fig. S7). We then examined baMTs that could be traced from the basal body to the lateral cell membrane.

A marked difference in the direction of baMTs was apparent between those extending from the basal body toward the anterior
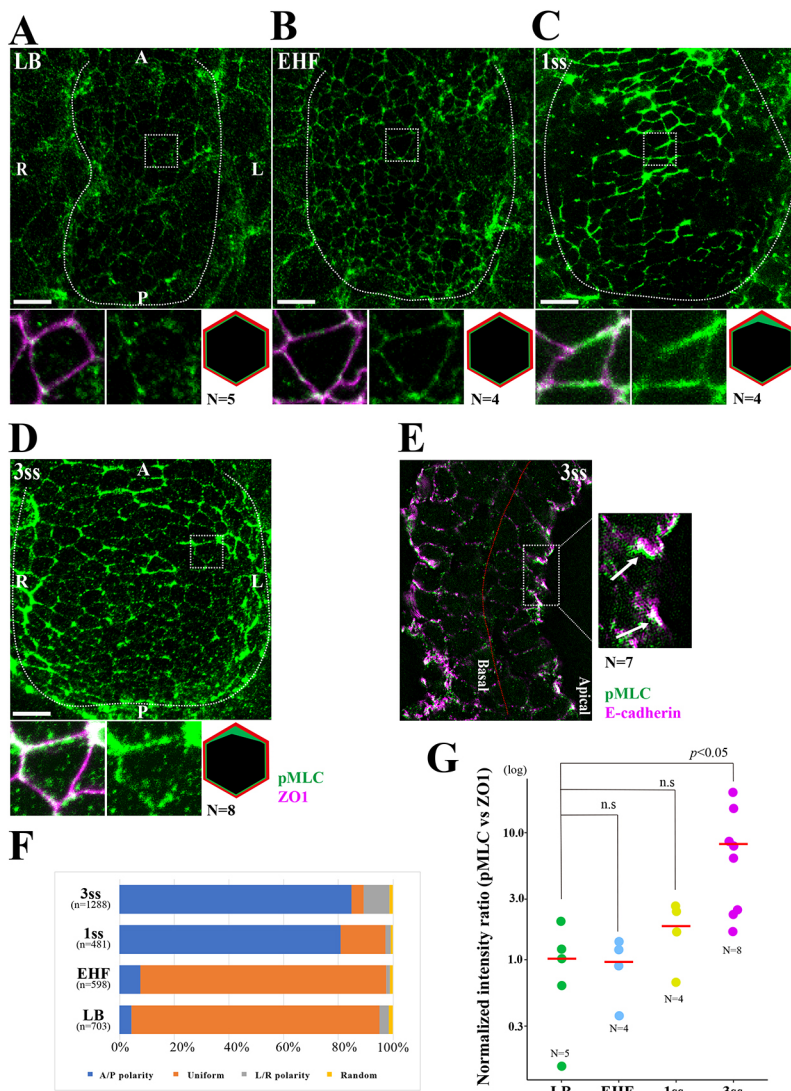
Fig. 5. Polarized localization of pMLC in node cells. (A-D) WT mouse embryos at the late bud (LB), early headfold (EHF), one-somite (1ss) and three-somite (3ss) stages were subjected to immunofluorescence staining with antibodies to pMLC (green) and to ZO1 (magenta), and the node region (enclosed within the white dashed line) was observed by super-resolution microscopy. The boxed regions in the upper panels are shown at higher magnification in the lower panels together with schematic representations of the pMLC and ZO1 staining patterns. pMLC signals are present at a low level and uniformly localized to the cell periphery of node cells at the late bud and early headfold stages, start to become compartmentalized to the anterior side of cells at the one-somite stage, and are polarized to the apical anterior side at the three-somite stage. (E) A sagittal section of the node from an embryo at the three-somite stage was stained with antibodies to pMLC (green) and to E-cadherin (magenta) and observed by super-resolution microscopy. The boxed region in the left panel is shown at higher magnification on the right. White arrows indicate specific localization of pMLC to the anterior edge of the node cells. Red line indicates the basal side of the node cells. (F) The frequency of cells showing the indicated pMLC staining pattern is summarized for four different developmental stages. The number of cells examined (n) is indicated for each stage. (G) The level of pMLC signals at the four different stages. The fluorescence intensity of pMLC at the node and that of ZO1 were measured as described in Materials and Methods. Normalized intensity ratio of pMLC was estimated as the ratio of the intensity of pMLC signals relative to that of ZO1 signals. Each dot denotes the embryo examined, with the red bars indicating mean values. For statistical significance, multiple group comparisons were performed by Dunnett's test. n.s, not significant. A, anterior; L, left; P, posterior; R, right. Scale bars: 10 μm (A-D); 5 μm (E).

side and those extending toward the posterior side at the two- to four-somite stage, with anterior baMTs extending horizontally and posterior baMTs extending vertically toward the basal side of the node cells (Fig. 9A). The termini of anterior baMTs appeared to reach the cell cortex, given that the termini of the MTs were located at the region positive for E-cadherin (Fig. 9A). This asymmetry in baMT pattern depended on developmental stage. The pattern thus did not show A-P asymmetry at the late bud stage but had become A-P asymmetric at the early headfold stage, when the basal body is still located centrally (Fig. 9A). The baMT pattern manifested more obvious A-P asymmetry at the two- to four-somite stage, when the basal body had shifted to the posterior side of the cell. Given that the asymmetry in baMTs develops earlier than the positional shift of the basal body, it is unlikely that the former is a consequence of the latter. Anteriorly polarized Vangl1 distribution was already apparent at the late bud stage (Fig. S8), when the baMT pattern remains symmetric (Fig. 9A), indicating that baMT organization becomes asymmetric after Vangl1 appears at the anterior side of node cells.

The length of baMTs on the anterior and posterior sides of node cells (leng-a and leng-p) as well as the extension angle relative to the apical membrane (ang-a and ang-p) were next quantitatively

analyzed (Fig. 9E). Although sagittal sections containing both the basal body and the entire length of baMTs were rare (Fig. S7), 123 baMTs in 24 cells from 12 embryos at the two- to four-somite stage, 66 baMTs in 16 cells from 10 embryos at the early headfold stage, and 66 baMTs in 20 cells from 10 embryos at the late bud stage were subjected to such analysis. There was no significant difference in length between anterior baMTs and posterior baMTs at any of the stages examined (Fig. S9). The angle of baMTs was symmetric between the anterior and posterior sides at the late bud stage (ang-a=ang-p), but it was asymmetric (ang-a<ang-p) at the early headfold and two- to four-somite stages (Fig. 10A-C).

The asymmetry in baMT organization was lost in pit cells of $Pk1^{-/-};Pk2^{-/-}$ embryos (Figs 9B and 10E) and $Dchs1^{-/-};Dchs2^{-/-}$ embryos (Fig. 9C) at the two- to four-somite stage as well as in WT embryos treated with ML-7 (Figs 9D and 10D), suggesting that it depends on the A-P polarized localization of PCP core proteins. Together, our results thus suggested that the organization of baMTs is asymmetric between the anterior and posterior sides of pit cells, that this asymmetry appears after Vangl1 localization becomes polarized and before the shift in basal body position, and that it requires the polarized localization of PCP core proteins such as Prickle and dachsous.
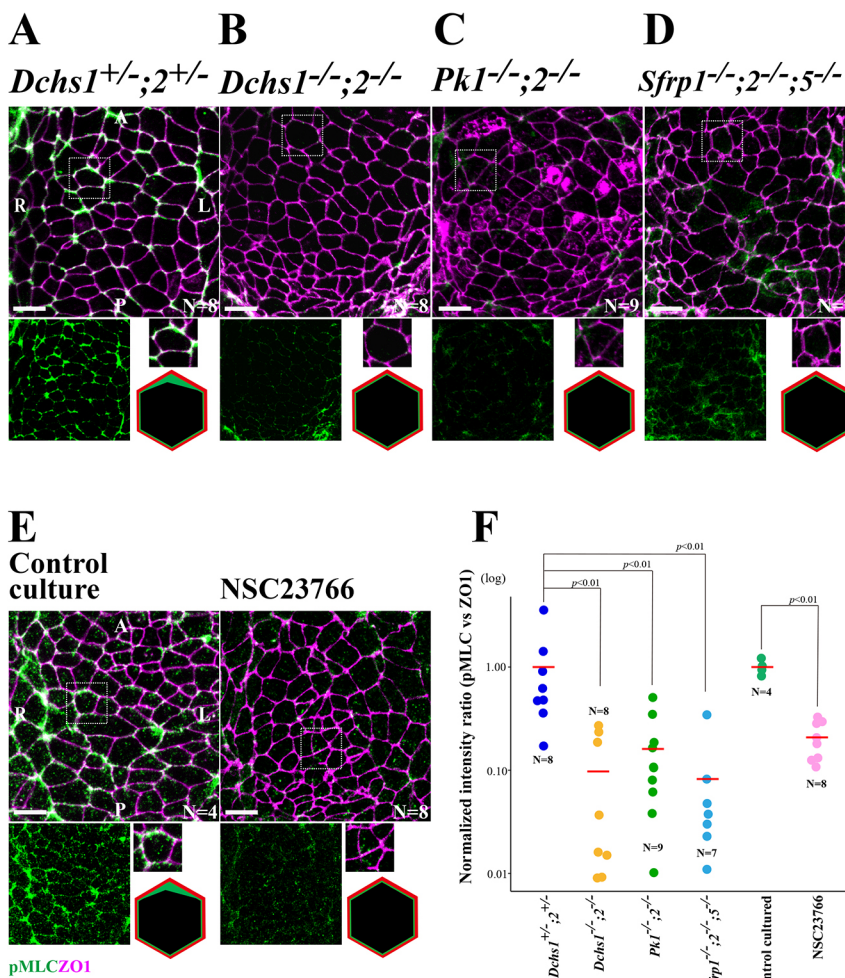
Fig. 6. Subcellular localization of pMLC in node cells of mutant embryos. (A-D) Immunofluorescence analysis of pMLC (green) and ZO1 (magenta) at the node of $Dchs1^{+/-};Dchs2^{+/-}$, $Dchs1^{-/-};Dchs2^{-/-}$, $Pk1^{-/-};Pk2^{-/-}$ and $Sfrp1^{-/-};Sfrp2^{-/-};Sfrp5^{-/-}$ embryos at the two- to three-somite stage. Only the node region is shown. The number of embryos examined (N) is indicated for each genotype. The boxed regions of the upper panels are shown in the insets together with schematic representations of the pMLC and ZO1 staining patterns. The anteriorly polarized localization of pMLC is impaired in the three mutants. (E) WT embryos at the late bud stage were cultured in the absence or presence of 150 µM NSC23766 for 10 h to allow their development to the two- to three-somite stage and were then stained for pMLC and ZO1. The number of embryos examined (N) is indicated. The boxed regions of the upper panels are shown below together with schematic representations of the pMLC and ZO1 staining patterns. The level of pMLC is reduced and its anterior localization is lost after treatment with the Rac1 inhibitor. (F) The level of pMLC signals at the node of the indicated embryos. Normalized intensity ratio of pMLC signals was estimated as the pMLC/ZO1 ratio (the intensity of pMLC signals relative to that of ZO1), as described in Fig. 5. Each dot denotes the embryo examined, with the red bars indicating mean values. Multiple group comparisons were performed by Dunnett's test. Statistical significance between control and NSC23766 was determined with unpaired Welch's test. A, anterior; P, posterior; R, right; L, left. Scale bars: 5 µm.

DISCUSSION

Role of dachsous in positioning of the basal body

We found that the anteriorly polarized localization of Vangl1 and the posterior positioning of the basal body were impaired in node cells of $Dchs1^{-/-};Dchs2^{-/-}$ embryos. Additional asymmetric events such as activation of actomyosin at the anterior side of the cell and the asymmetric organization of baMTs were also impaired in the mutant embryos. However, Dchs1 and Dchs2 were found to be localized at the apical side of the cell without A-P polarity. Unlike in the *Drosophila* wing, where Dachsous is localized in a polarized manner (Hale and Strutt, 2015), Dchs1 and Dch2 likely have a permissive role in polarization of node cells in the mouse.

Physical mechanism underlying the shift in basal body position: role of baMT asymmetry

Given that MTs and actomyosin play a role in PCP in other contexts, it is not surprising that we found that both are essential for correct positioning of the basal body in node pit cells. Our experiments with various inhibitors suggested that, not only the total amount of MTs and F-actin but also their proper dynamics are required for translocation of the basal body toward the posterior side as well as for maintenance of its position at this side.

What mechanism might be responsible for the shift in the basal body from its initial central position to its subsequent posterior position? Although we have genetically dissected this mechanism, its physical manifestation remains unclear. It is likely that the basal

body is moved by force, but what type of force (pulling or pushing) might be involved and how is this force generated by MTs and actomyosin? Theoretically, the basal body may be pushed or pulled toward the posterior side (Zhu et al., 2010). In the case of the migration of the male pronucleus of sea urchin or *Caenorhabditis elegans* toward the center of the egg after fertilization, it has been suggested that a mechanism dependent on cytoplasmic dynein provides a pulling force dependent on MT length, with more force generated by the longer front-facing MTs than by the shorter rear- or cortex-facing MTs (Kimura and Onami, 2005; Tanimoto et al., 2016, 2018). However, we found that the length of baMTs in mouse node cells did not differ between those on the anterior or posterior sides. Moreover, cytoplasmic dynein does not appear to contribute to the shift in basal body position, given that this shift was unaffected by ciliobrevin D. It is therefore unlikely that a pulling force dependent on MT length and driven by cytoplasmic dynein mediates the positional shift of the basal body. Alternatively, baMTs may provide a pushing force on the basal body either through the action of plus end-directed kinesin motors that are anchored to stable structures in the cell, or through interaction between the termini of MTs and the cell cortex coupled with MT plus-end dynamics. If the same absolute level of pushing force is generated by anterior baMTs and posterior baMTs, the difference in the angle between these MTs (ang-a versus ang-p) would result in a greater pushing force on the basal body generated by those on the anterior side than by those on the posterior side (with regard to the A-P axis component of the
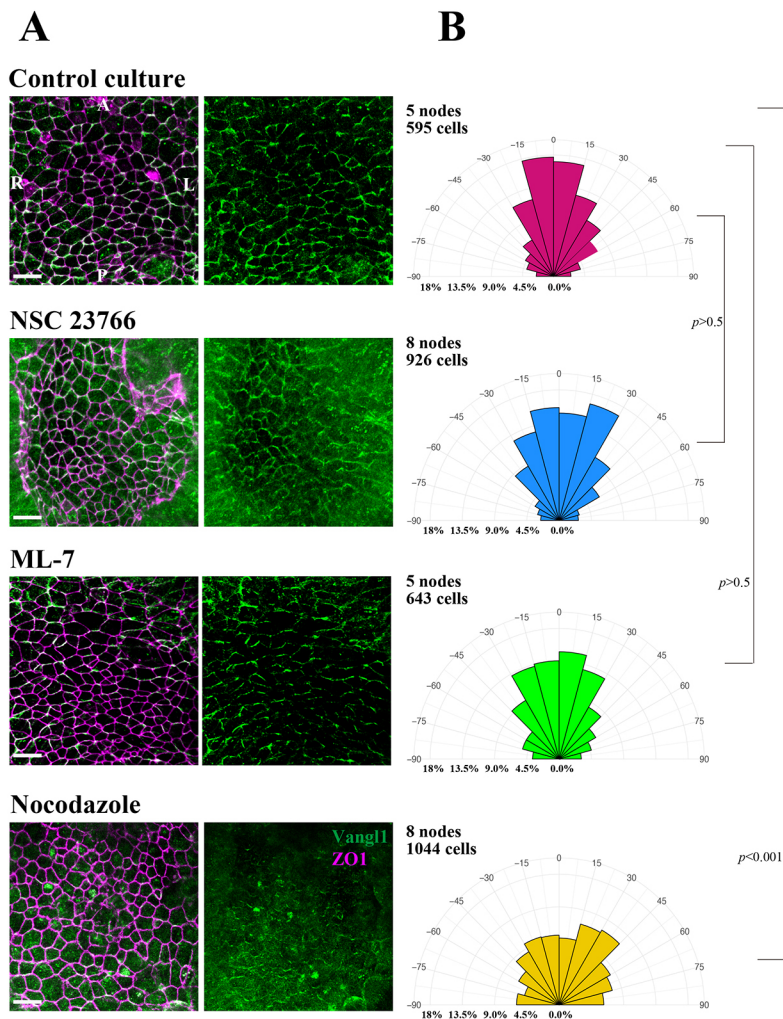
A

B

Fig. 7. Subcellular localization of Vangl1 in node cells treated with various inhibitors. (A) Immunofluorescence localization of Vangl1 in node cells of mouse embryos cultured with NSC23766, ML-7 or nocodazole from the LB stage to the two- to three-somite stage. The node region is shown for each embryo. The L-R and A-P axes are indicated. The polarized distribution of Vangl1 in node cells was maintained by ML-7 and NSC23766 but was impaired by nocodazole. (B) Quantitative analysis of the Vangl1 localization pattern in node cells of embryos cultured with the indicated inhibitor. The angle (–90° to +90°) in the rose diagrams was determined by quantitative analysis for each cell and is categorized into 12 classes (15° for each class). The length of each bar indicates the cell number for each class. The number of cells analyzed was 595 from five control embryos, 926 from eight embryos cultured with NSC23766, 643 from five embryos cultured with ML-7; 1044 from eight embryos cultured with nocodazole and. The *P*-values were determined with Mardia-Watson-Wheeler test and were adjusted using Bonferroni correction. Scale bars: 10 µm.

force vector, Fa>Fp) (Fig. 10F). In addition to the difference in angle, differential dynamics or differential interaction with the cortex of anterior and posterior baMTs may further contribute to the asymmetry in pushing force. If baMTs on the anterior side are more dynamic than those on the posterior side, this difference may result in the generation of a greater pushing force on the anterior side. However, there was no significant difference between leng-a and leng-p. A higher pushing force could also be generated toward the posterior side if baMTs interact with the cell cortex only on the anterior side. However, our observations at the resolution level of microscopy applied indicated that the termini of both anterior and posterior baMTs are localized to the cell cortex. Together, our results suggest that the difference in the angle between anterior and posterior baMTs may generate a pushing force that is able to move the basal body toward the posterior side.

Mechanism underlying asymmetric baMT organization along the A-P axis

PCP-dependent regulation of the asymmetric organization of baMTs has been described in ciliated epithelial cells of *Xenopus*, in which a gap between MTs and the cell cortex is present at the anterior side of the cell but not at the posterior side (Kim et al., 2018). What mechanism might be responsible for the asymmetric organization of baMTs in mouse pit cells, with anterior and posterior baMTs extending horizontally and vertically,

respectively? The organization of baMTs in pit cells becomes asymmetric at the early headfold stage, before the basal body has shifted to the posterior side of the cell, indicating that the asymmetry in baMT pattern is not a consequence of this posterior shift of the basal body. Given that the baMT asymmetry was apparent only after the anterior localization of Vangl1 and was impaired in Pk and Dchs mutant embryos, it is dependent on PCP proteins, in particular those present at the anterior side of pit cells, such as Pk. Of interest, Vangl1 and E-cadherin, as well as the termini of baMTs, were found to be localized at the cell cortex on the anterior side of pit cells. Although it remains to be determined whether the termini of anterior baMTs interact with Vangl1, it is possible that they are anchored by Vangl1-Pk-Dchs proteins at the cell cortex on the anterior side of pit cells. If this is the case, such anchoring of baMTs would not occur on the posterior side of pit cells, which would render baMT organization asymmetric. However, there is no direct evidence to date for a physical interaction between MTs and PCP proteins at a molecular level in any organism.

Cooperation between MTs and actomyosin

Anisotropic activation of myosin II by PCP has been described in association with several cellular phenomena. For example, PCP proteins compartmentalize active myosin II along the A-P axis of *Xenopus* notochord cells for convergent extension (Shindo and Wallingford, 2014). For positioning of the basal body in node cells,
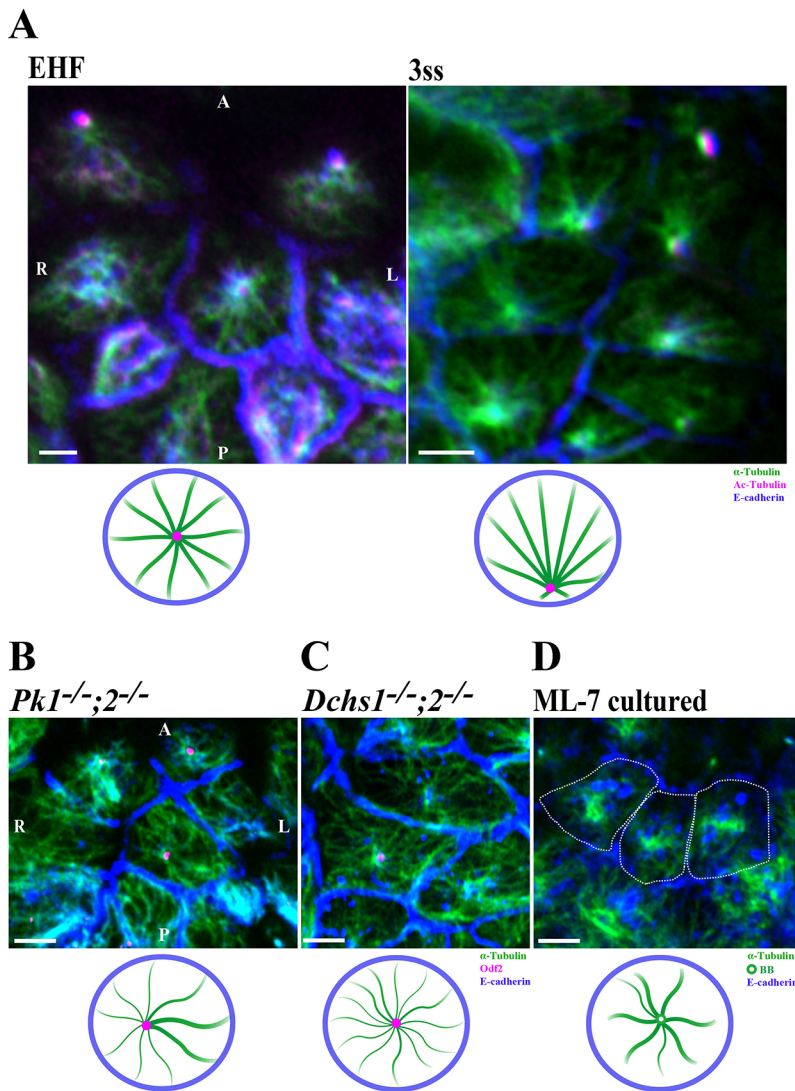
Fig. 8. Regulation of baMT asters in node cells by PCP core proteins. (A-D) WT embryos at the early headfold (EHF) and three-somite (3 ss) stages (A), $Pk1^{-/-};Pk2^{-/-}$ (B) and $Dchs1^{-/-}$; $Dchs2^{-/-}$ (C) embryos at the three-somite stage, and WT embryos cultured with ML-7 (25 µM) from the late bud stage to the three-somite stage (D) were stained for α-tubulin (green), E-cadherin (blue), and either acetylated (Ac-) tubulin (A) or Odf2 (B-D). Ventral views and schematic representations are shown. The white dashed lines in D indicate the cell boundary. The baMT aster is composed of straight MT fibers radiating from the basal body to the cell periphery in the WT embryos, but it is disorganized, being composed of curved MT fibers, in the mutant embryos (B,C) or highly truncated in the ML-7-treated WT embryo (D). baMT fibers to the anterior side of the cell appear to be longer than those to the posterior side in the WT embryo at the three-somite stage (A) because of the angle of observation (ventral view). Such is not the case in sagittal sections of node cells (Fig. S8). A, anterior; L, left; P, posterior; R, right. Scale bars: 2 µm.

actomyosin likely provides a pushing force on the basal body, given that activation of myosin II was detected on the anterior side of pit cells. This polarized activation of myosin II may depend on Vangl-Rac1 interaction. During neural tube closure in chick, the PCP protein Celsr1 at adherens junctions is oriented along the mediolateral axis of the cell and cooperates with the Rho guanine nucleotide exchange factor PDZ-RhoGEF to upregulate Rho kinase, leading to actomyosin-dependent anisotropic contraction (Nishimura et al., 2012). In the developing neural tube of mouse embryos, Vangl2 interacts with Rac1 and recruits it to adherens junctions (Lindqvist et al., 2010). Similarly, Vangl1 present at the anterior side of node cells may target Rac1 activity to adherens junctions on the anterior side, where it activates actomyosin.

How might MTs and actomyosin cooperate to shift the basal body of pit cells? MTs and actomyosin function together in many cellular processes including cell migration, cell polarization and cell division. Apical constriction of bottle cells in gastrulating *Xenopus* embryos is driven by both actomyosin contractility and MTs, although the precise role of MTs in this process is unknown (Lee and Harland, 2007). With regard to the change in position of the basal body in pit cells, actomyosin-driven force may result in constriction of the anterior side of pit cells, which could provide a pushing force via MTs linking the cell cortex and the basal body.

However, the shape of pit cells does not change between before and after the positional shift of the basal body (Hashimoto et al., 2010; Minegishi et al., 2017). Alternatively, activation of myosin II may stimulate baMT plus-end dynamics on the anterior side, which could provide a pushing force via these baMTs.

In all, our study has dissected the mechanism of basal body positioning in node pit cells during L-R symmetry breaking in the mouse embryo. Our results implicate MTs and actomyosin, in particular the PCP-regulated asymmetric organization of baMTs, in this process. However, the precise nature of the mechanical force responsible for the change in the position of the basal body requires further study.

MATERIALS AND METHODS
Mouse strains
All mouse experiments were performed in accordance with guidelines of the RIKEN Center for Biosystems Dynamics Research and in compliance with an institutional license (A2016-01-6). Mice were maintained in the animal facility of the RIKEN Center for Biosystems Dynamics Research. $Pk1^{-/-}$; $Pk2^{-/-}$ mutant mice (which lack exon 6 of each gene) have been described previously (Minegishi et al., 2017). The *Dchs1* mutant allele was generated with the CRISPR/Cas9 system, with the region encompassing exon 2 to exon 7 being deleted with the small guide RNAs ΔEx2 gRNA1 and ΔEx7 gRNA2 [5′-GATAGAAATGGATGAGCTGC*TGG*-3′ and
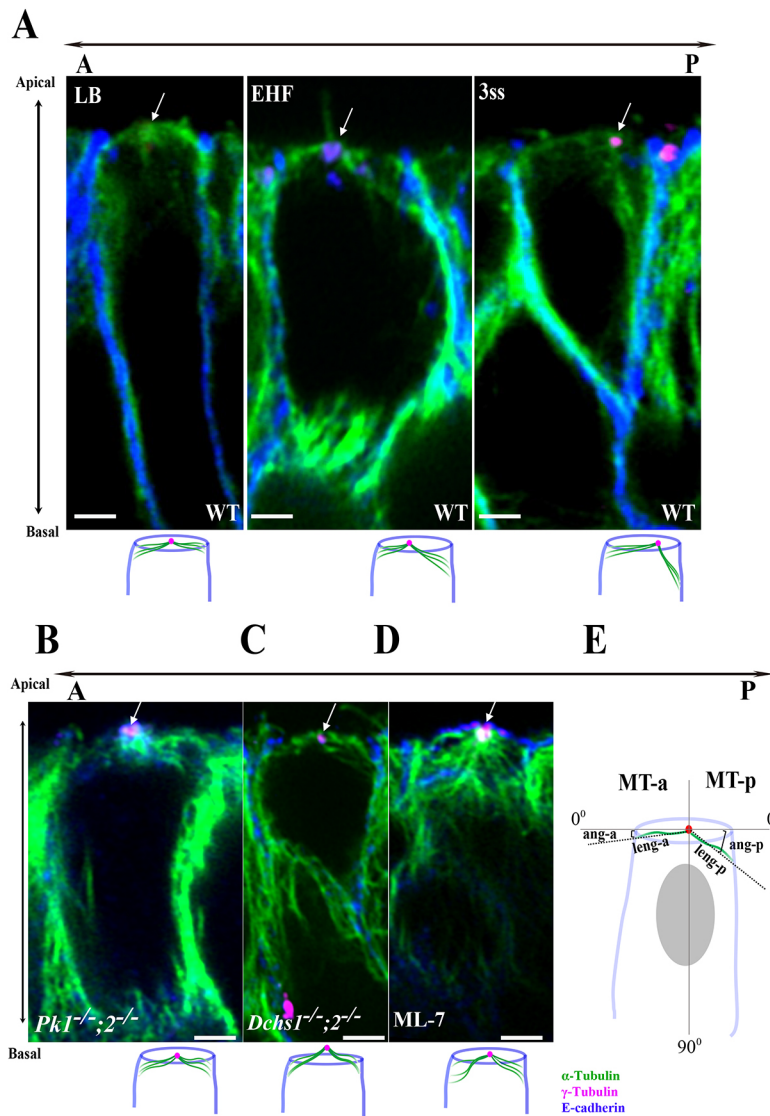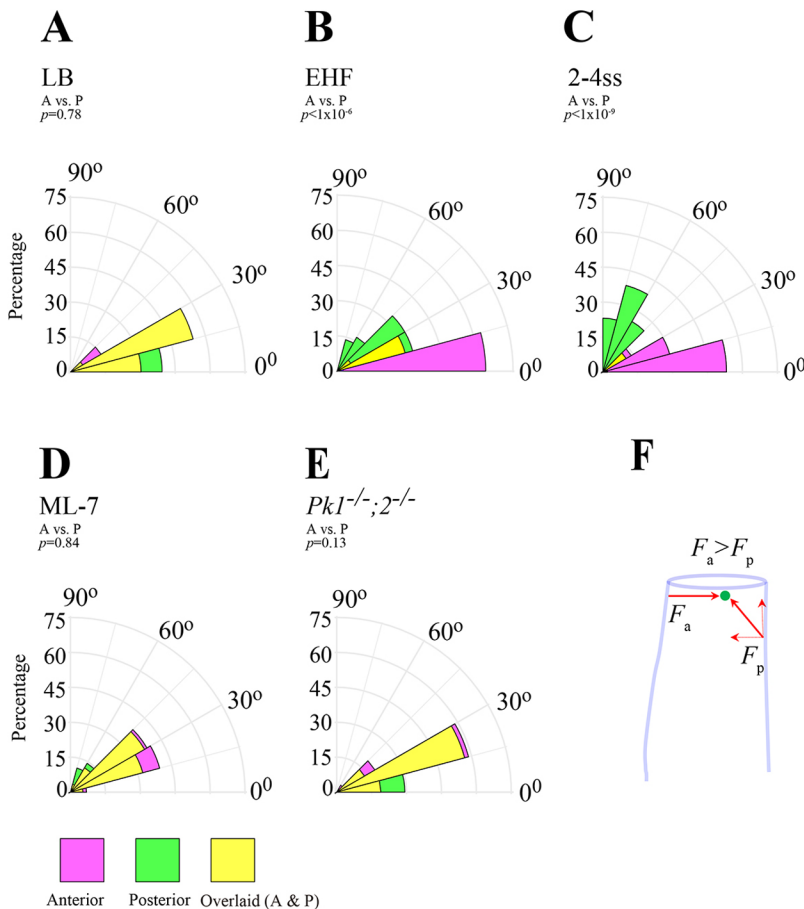
DEVELOPMENT

Fig. 9. A-P asymmetric organization of baMTs in node cells.
(A-D) Sagittal sections through the node of WT embryos at the late bud (LB), early headfold (EHF) and three-somite (3ss) stages (A), of $Pk1^{-/-};Pk2^{-/-}$ (B) or $Dchs1^{-/-};Dchs2^{-/-}$ (C) embryos at the three-somite stage, and of a WT embryo treated with ML-7 (25 µM) from the late headfold to three-somite stage (D), were stained with antibodies to α-tubulin (green), to γ-tubulin (magenta) and to E-cadherin (blue) and then observed by super-resolution microscopy. White arrows indicate the position of the basal body. Schematic representations show the position of the basal body and organization of baMTs. The A-P asymmetric organization of baMTs is apparent at the early headfold and three-somite stages for WT embryos (A), but was lost in the mutant embryos (B,C) and the ML-7-treated WT embryo (D). The frequency of node cells with asymmetric baMTs was 2/20 at the LB stage, 15/16 at the EHF stage, 24/24 at the three somite stage, 2/23 in $Pk1^{-/-};2^{-/-}$ embryos, 0/15 in $Dchs1^{-/-};2^{-/-}$ embryos and 3/22 in ML-7-treated embryos (summarized in Fig. S9C). (E) Schematic showing how the length (leng-a, leng-p) and angle (ang-a, ang-p) of MT bundles were measured. Leng-a and leng-p are defined as the linear distance from the basal body to the ends of anterior (baMT-a) or posterior (baMT-p) baMTs, respectively. Ang-a and ang-p are defined as the angle between the apical membrane and baMT-a or baMT-p, respectively. The A-P axis is at the 0° level and the dorsoventral axis is 90° to the A-P axis. Scale bars: 2 µm.

5′-*CCT*CCTGGAACAGGTATAAGACA-3′, respectively, with the proto-spacer adjacent motif (PAM) domains being indicated in italics]. *Cas9* mRNA and the small guide RNAs were generated by *in vitro* transcription with the use of an SP6 mMessage mMachine kit (AM1340, Ambion), with minor modifications to the recommended protocol, and they were injected into fertilized eggs obtained from C57BL/6 mice. The genotypes of *Dchs1* mutant pups were confirmed by polymerase chain reaction (PCR) with the primers ex2_F (5′-CCCGTAAAGTTGGAGATGGA-3′), ex2_WT_R (5′-GCACTGTAGCCCCTAACAGC-3′) and ex7_MT_R (5′-TCCTGCCCCATACCAGTTAG-3′). The sizes of the PCR products for the WT and mutant alleles were 442 and 320 bp, respectively. Sequences were confirmed by DNA-sequencing analysis. For generation of the *Dchs2* mutant allele, an FRT-*Pgk-neo*-FRT-loxP cassette was inserted upstream of exon 29, and a single loxP site was inserted downstream of this exon. The targeted exon and the *neo* cassette were removed with *CAG-Cre* and *CAG-Flp* transgenic mice. A similar mutant allele of *Dchs2* lacking exon 29 has been described previously (Bagherie-Lachidan et al., 2015). The genotypes of *Dchs2* mutant pups were confirmed by PCR analysis with the primers Dchs2-WT-F (5′-CTTGATGTAAGGCTGCGATG-3′) and Dchs2-WT-R (5′-CAAACTTCAAAAGTGGACATTGAG-3′) for the WT allele (with the size of the PCR product being 230 bp) and with Dchs2-WT-F and Dchs2-Mut-R (5′-GGTGGGGCACAATCTAGAAA-3′) for the mutant allele (with the size of the PCR product being 420 bp). Sequences were confirmed by DNA-sequencing analysis. $Dchs1^{-/-}$; $Dchs2^{-/-}$ mice were obtained by

mating *Dchs1* and *Dchs2* mutant mouse lines. The $Dchs2^{Venus}$ allele encoding a Dchs2::Venus fusion protein in which Venus is linked to the COOH-terminus of Dchs2 was generated in embryonic stem cells (ESCs) with the use of the CRISPR/Cas9 system and with a targeting vector, an expression vector encoding Cas9, and small guide RNAs (5′-CACCGAAAGCTGAAGATGAAGTTCA*AGG*-3′ and 5′-AAACT-GAACTTCATCTTCAGCTTT*CCT*-3′, with the PAM indicated in italics). ESCs with the $Dchs2^{Venus/+}$ genotype were used to generate $Dchs2^{Venus/+}$ mice. The genotype of $Dchs2^{Venus/+}$ pups was confirmed by PCR analysis with the primers Dchs2-F (5′-CAGGTCACCAATGTTGCCAGATGG-3′) and Dchs2-R (5′-CGCTGGCTACATGAGATAGTCTGC-3′) for the WT allele, and Dchs2-F and Dchs2-Venus-R (5′-GAAGTCGTGCTGCTTCATGTGGTC-3′) for the $Dchs2^{Venus}$ allele.

Immunofluorescence analysis

Dissected embryos were fixed with 4% paraformaldehyde for 30 min on ice, dehydrated with methanol or permeabilized for 20 min at room temperature with 0.2% Triton X-100 in phosphate-buffered saline (PBS). For immunofluorescence staining of pMLC, embryos were instead fixed for 30 min on ice with 4% paraformaldehyde in PBS also containing 0.5% Triton X-100 and 50 nM calyculin A before immunostaining. All embryos were then stained overnight at 4°C with the following primary antibodies at the indicated dilutions: E-cadherin (mouse monoclonal, 1:100; TaKaRa, M108), Ser[19]-phosphorylated myosin light chain 2 (rabbit polyclonal, 1:100; Cell Signaling

Fig. 10. Asymmetry in baMT organization as revealed by quantitative analysis. (A-E) Rose diagrams showing the angles of baMT bundles (0° to 90° for ang-a and ang-p) in pit cells of WT embryos at the late bud (LB), early headfold (EHF), and two- to four-somite (2-4ss) stages, following treatment with ML-7 (25 µM) from the late headfold to three-somite stage, and of $Pk1^{-/-};Pk2^{-/-}$ embryos at the two- to four-somite stage. Angles are classified into six classes (15° for each class). The area for each class indicates the number of MT bundles, with magenta and green areas representing ang-a and ang-p, respectively, and yellow areas representing overlay of ang-a and ang-p. The P-values for comparisons between ang-a and ang-p were determined with Tukey's honest significance test. (F) Schematic model to account for how the difference in the angle of baMTs between the anterior and posterior sides of a node cell might generate differential pushing forces on the anterior (Fa) and posterior (Fp) sides. See text for further details.

Technology, 3675), ZO1 (mouse monoclonal clone ZO1-1A12, 1:200; Invitrogen), Odf2 (rabbit polyclonal, 1:200; Abcam, ab43840), Vangl1 (rabbit polyclonal, 1:200; Sigma-Aldrich, HPA025235), γ-tubulin (clone GTU-88, mouse monoclonal, 1:200; Sigma-Aldrich, T5326), Vangl2 (rabbit polyclonal, 1:250; Sigma-Aldrich, HPA027043), GFP (chicken polyclonal, 1:300; Abcam, ab13970), Dchs1 (rabbit polyclonal, 1:100; kindly provided by Masatoshi Takeichi, RIKEN Center for Biosystems Dynamics Research, Japan) and active Rac1 (mouse monoclonal, 1:500; NewEast Bioscience, 26903). Fluorescein isothiocyanate (FITC)-conjugated α-tubulin antibodies (mouse monoclonal, 1:100; Sigma-Aldrich, F2168) and Alexa Fluor 568-labeled Phalloidin (1:50, Thermo Fisher Scientific, A12380) were also used to detect to α-tubulin and F-actin, respectively. The embryos were washed with PBS containing 0.01% Triton X-100 before exposure to Alexa Fluor-conjugated secondary antibodies. The following secondary antibodies were used: Alexa Fluor 568, goat anti-mouse IgG H&L (Invitrogen, A11004, 1:200), Alexa Fluor 488, goat anti-rabbit IgG H&L (Invitrogen, A11034, 1:200), Alexa Fluor 594, goat anti-rabbit IgG H&L (Abcam, ab150084, 1:200), Alexa Fluor 488, goat anti-chicken IgY H&Y preadsorbed (Abcam, ab150173, 1:500), Alexa Fluor 594, donkey anti-rat IgG H&L preadsorbed (Abcam, ab150156, 1:200), Alexa Fluor 647, donkey anti-rat IgG H&L (Abcam, ab150159, 1:200) and Alexa Fluor 488, goat anti-mouse IgM mu chain (Abcam, ab150121, 1:500). The node of stained embryos was excised, placed on a glass slide with silicone rubber spacers, covered with a cover glass and imaged with an FV-3000 confocal microscope (Olympus). For immunofluorescence staining of microtubules, embryos were dissected in Hepes-buffered Dulbecco's modified Eagle's medium (pH 7.2) warmed to 37°C and were fixed for 30 min at 37°C with 4% paraformaldehyde in PEM buffer [100 mM Pipes-KOH (pH 6.9), 5 mM EDTA, 5 mM MgCl₂] containing 50 mM sorbitol and 0.2% Triton X-100. They were washed twice in PBS containing 0.01% Triton X-100 for whole-embryo imaging as described previously (Minegishi et al., 2017). For preparation of frozen sections of the node, the embryos were transferred to a series of sucrose solutions (15-30%) and then frozen in OCT compound (Sakura Finetek).

Sections were cut at a thickness of 4-5 µm using a CRYOSTAR NX70 instrument (Thermo Fisher Scientific) and then immunostained as described previously (Toya et al., 2016). Immunostained specimens were sealed with ProLong Glass Antifade Mountant (P36983, Invitrogen) and images were acquired using a Zeiss LSM880 microscope equipped with Airyscan laser scanning confocal microscope equipped with an Axio Observer Z1 inverted microscope, using a Plan-APOCHROMAT 63× Oil for SR objective lens (Zeiss).

Observation of nodal flow by PIV analysis
Nodal flow was observed by multipoint scanning confocal microscopy. Particle image velocimetry (PIV) analysis was performed as described previously (Minegishi et al., 2017; Shinohara et al., 2012). Recovered embryos were first cultured under 5% CO₂ for 30 min at 37°C in Dulbecco's modified Eagle's medium (DMEM) supplemented with 75% rat serum. The region containing the node was then excised and the node cavity was filled with DMEM supplemented with 10% fetal bovine serum and 0.2 µm diameter fluorescent microbeads (Invitrogen, F8811). The motion of the beads was monitored for 10 s in planes of +5 and +10 µm relative to the cavity (21 frames per second) with the use of a CSU-W1 confocal unit (Yokogawa) and an iXon-Ultra EMCCD camera (Andor Technology) connected to an IX83 microscope (Olympus) fitted with a 60× objective lens. Time-series images for PIV analysis were captured at a resolution of 512 by 512 pixels and were processed with interrogation windows of 16 by 16 pixels with 50% overlap, corresponding to a spatial resolution of 4.3 by 4.3 mm. The time-averaged velocity distributions were calculated for 10 s intervals.

Quantitative analysis of basal body position
The ABP, representing the relative position of the basal body in each node cell along the A-P axis (vertical), was analyzed as described previously (Hashimoto et al., 2010). Confocal images of the node stained with antibodies to Odf2 and to ZO1 were obtained to determine the position of the

basal body in each node cell. For characterization of the shape and orientation of node cells, the outline of each cell was calculated from the pattern of ZO1 staining, with the use of an ImageJ software plugin (http://rsb.info.nih.gov/nih-image) to apply watershed segmentation. The basal body was traced manually according to the Odf2 staining image, and the x and y coordinates of each basal body were recorded with the use of the graphical user interface of MATLAB software. The relative value for the position of the basal body in each cell was calculated from the coordinate data with the anterior and posterior ends of the cell expressed as −1.0 and +1.0, respectively.

Quantitative analysis of Vangl1 distribution in node cells
The node region stained with antibodies to Vangl1 and to ZO1 was observed by super-resolution microscopy. The angle of Vangl1 localization in node cells was measured as described previously (Minegishi et al., 2017; Shi et al., 2016). Rose diagrams were drawn with the use of R(RStudio) software. Statistical analysis was performed with the Mardia-Watson-Wheeler test.

Quantitative analysis of pMLC signals
To estimate the intensity of pMLC, Z-stack projection images were converted to the average image using Fiji (ImageJ). The region of interest (ROI) was defined on the average image and the membrane domain was extracted from ROI by applying mask function on the ZO1 image. After subtracting background signals, the sum of the intensity was calculated for pMLC and ZO1, and was corrected by the differences in laser power and HV value. Finally, the normalized pMLC/ZO1 ratiometric value was estimated using the average value of the LB embryos (in Fig. 5G) and that of control embryos (in Fig. 6F) as a reference.

Whole-embryo culture and inhibitor treatment
Embryos were dissected into Phenol Red-free DMEM supplemented with 10% fetal bovine serum (Invitrogen). Those at the late headfold stage or three-somite stage were selected and cultured by the roller culture method under 5% CO_2 at 37°C in 50 ml tubes containing DMEM supplemented with 75% rat serum. Inhibitors were added to the medium at final concentrations of 30 µM or 100 nM for nocodazole (M1404, Sigma-Aldrich), 25 µM for ML-7 (ab120848, Abcam), 25 µM for (±)blebbistatin (ab120425, Abcam), 150 µM for NSC23766 (ab142161, Abcam), 3 µM for jasplakinolide (ab141409, Abcam), 0.5 µM for latrunculin A (AG-CN2-0027-C100, Funakoshi), 40 µM for ciliobrevin D (250401, Sigma-Aldrich), 5 µM for Taxol (ab143553, Abcam) and 30 µM for Y-27632 (257-00511, Wako). Embryos were allowed to develop from the late headfold to three-somite stage, or from the three-somite to five-somite stage, and were then fixed for immunofluorescence staining of ZO1 and Odf2. In some experiments, embryos were cultured from the late bud stage.

Analysis of baMT images
Sagittal sections of embryos through the middle of the node were stained with antibodies to γ-tubulin or to Odf2, to α-tubulin and to E-cadherin to determine the position of the basal body, microtubule asters and the cell boundary, respectively, in each node cell. The length of baMTs on the anterior and posterior sides of each cell (leng-a and leng-p, respectively) were measured from the α-tubulin signal with the use of FIJI (ImageJ). Leng-a and leng-p were defined as the linear distance between the basal body and the end of the α-tubulin signal at the E-cadherin-positive area. After the length of all visible baMTs was measured in two-dimensional images, the average leng-a and leng-p values and their ratio (leng-a/leng-p) were estimated for each cell. The angle of baMTs relative to the apical plane was measured for those on the anterior and posterior sides of each node cell (ang-a and ang-p, respectively).

Competing interests
The authors declare no competing or financial interests.

Author contributions
Methodology: T.A.K., T.K.; Software: T.A.K.; Formal analysis: X.S., K. Minegishi; Investigation: X.S., H.N., E.K.; Resources: H.S., K.T.; Data curation: X.S., K. Mizuno; Writing - original draft: X.S., H.H.; Visualization: Y.I.; Supervision: H.H.

Peer review history
The peer review history is available online at https://journals.biologists.com/dev/article-lookup/doi/10.1242/dev.200315.

References
Antic, D., Stubbs, J. L., Suyama, K., Kintner, C., Scott, M. P. and Axelrod, J. D. (2010). Planar cell polarity enables posterior localization of nodal cilia and left-right axis determination during mouse and Xenopus embryogenesis. *PLoS ONE* **5**, e8999. doi:10.1371/journal.pone.0008999

Bagherie-Lachidan, M., Reginensi, A., Pan, Q., Zaveri, H. P., Scott, D. A., Blencowe, B. J., Helmbacher, F. and McNeill, H. (2015). Stromal Fat4 acts non-autonomously with Dchs1/2 to restrict the nephron progenitor pool. *Development* **142**, 2564-2573. doi:10.1242/dev.122648

Blum, M., Feistel, K., Thumberger, T. and Schweickert, A. (2014). The evolution and conservation of left-right patterning mechanisms. *Development* **141**, 1603-1613. doi:10.1242/dev.100560

Crespo-Enriquez, I., Hodgson, T., Zakaria, S., Cadoni, E., Shah, M., Allen, S., Al-Khishali, A., Mao, Y., Yiu, A., Petzold, J. et al. (2019). Dchs1-Fat4 regulation of osteogenic differentiation in mouse. *Development* **146**, dev176776. doi:10.1242/dev.176776

Devenport, D. (2014). The cell biology of planar cell polarity. *J. Cell Biol.* **207**, 171-179. doi:10.1083/jcb.201408039

Devenport, D. (2016). Tissue morphodynamics: translating planar polarity cues into polarized cell behaviors. *Semin. Cell Dev. Biol.* **55**, 99-110. doi:10.1016/j.semcdb.2016.03.012

Dogterom, M. and Koenderink, G. H. (2019). Actin-microtubule crosstalk in cell biology. *Nat. Rev. Mol. Cell Biol.* **20**, 38-54. doi:10.1038/s41580-018-0067-1

Durst, R., Sauls, K., Peal, D. S., deVlaming, A., Toomer, K., Leyne, M., Salani, M., Talkowski, M. E., Brand, H., Perrocheau, M. et al. (2015). Mutations in DCHS1 cause mitral valve prolapse. *Nature* **525**, 109-113. doi:10.1038/nature14670

Goodrich, L. V. and Strutt, D. (2011). Principles of planar polarity in animal development. *Development* **138**, 1877-1892. doi:10.1242/dev.054080

Hale, R. and Strutt, D. (2015). Conservation of planar polarity pathway function across the animal kingdom. *Annu. Rev. Genet.* **49**, 529-551. doi:10.1146/annurev-genet-112414-055224

Harumoto, T., Ito, M., Shimada, Y., Kobayashi, T. J., Ueda, H. R., Lu, B. and Uemura, T. (2010). Atypical cadherins Dachsous and Fat control dynamics of noncentrosomal microtubules in planar cell polarity. *Dev. Cell* **19**, 389-401. doi:10.1016/j.devcel.2010.08.004

Hashimoto, M., Shinohara, K., Wang, J., Ikeuchi, S., Yoshiba, S., Meno, C., Nonaka, S., Takada, S., Hatta, K., Wynshaw-Boris, A. et al. (2010). Planar polarization of node cells determines the rotational axis of node cilia. *Nat. Cell Biol.* **12**, 170-176. doi:10.1038/ncb2020

Kim, S. K., Zhang, S., Werner, M. E., Brotslaw, E. J., Mitchell, J. W., Altabbaa, M. M. and Mitchell, B. J. (2018). CLAMP/Spef1 regulates planar cell polarity signaling and asymmetric microtubule accumulation in the Xenopus ciliated epithelia. *J. Cell Biol.* **217**, 1633-1641. doi:10.1083/jcb.201706058

Kimura, A. and Onami, S. (2005). Computer simulations and image processing reveal length-dependent pulling force as the primary mechanism for C. elegans male pronuclear migration. *Dev. Cell* **8**, 765-775. doi:10.1016/j.devcel.2005.03.007

Lee, J.-Y. and Harland, R. M. (2007). Actomyosin contractility and microtubules drive apical constriction in Xenopus bottle cells. *Dev. Biol.* **311**, 40-52. doi:10.1016/j.ydbio.2007.08.010

Liao, G., Nagasaki, T. and Gundersen, G. G. (1995). Low concentrations of nocodazole interfere with fibroblast locomotion without significantly affecting microtubule level: implications for the role of dynamic microtubules in cell locomotion. *J. Cell Sci.* **108**, 3473-3483. doi:10.1242/jcs.108.11.3473

Lindqvist, M., Horn, Z., Bryja, V., Schulte, G., Papachristou, P., Ajima, R., Dyberg, C., Arenas, E., Yamaguchi, T. P., Lagercrantz, H. et al. (2010). Vang-like protein 2 and Rac1 interact to regulate adherens junctions. *J. Cell Sci.* **123**, 472-483. doi:10.1242/jcs.048074

DEVELOPMENT

Mao, Y., Mulvaney, J., Zakaria, S., Yu, T., Morgan, K. M., Allen, S., Basson, M. A., Francis-West, P. and Irvine, K. D. (2011). Characterization of a Dchs1 mutant mouse reveals requirements for Dchs1-Fat4 signaling during mammalian development. *Development* **138**, 947-957. doi:10.1242/dev.057166

Mao, Y., Kuta, A., Crespo-Enriquez, I., Whiting, D., Martin, T., Mulvaney, J., Irvine, K. D. and Francis-West, P. (2016). Dchs1-Fat4 regulation of polarized cell behaviours during skeletal morphogenesis. *Nat. Commun.* **7**, 11469. doi:10.1038/ncomms11469

Minegishi, K., Hashimoto, M., Ajima, R., Takaoka, K., Shinohara, K., Ikawa, Y., Nishimura, H., McMahon, A. P., Willert, K., Okada, Y. et al. (2017). A Wnt5 activity asymmetry and intercellular signaling via PCP proteins polarize node cells for left-right symmetry breaking. *Dev. Cell* **40**, 439-452.e34. doi:10.1016/j.devcel.2017.02.010

Nishimura, T., Honda, H. and Takeichi, M. (2012). Planar cell polarity links axes of spatial dynamics in neural-tube closure. *Cell* **149**, 1084-1097. doi:10.1016/j.cell.2012.04.021

Nonaka, S., Tanaka, Y., Okada, Y., Takeda, S., Harada, A., Kanai, Y., Kido, M. and Hirokawa, N. (1998). Randomization of left-right asymmetry due to loss of nodal cilia generating leftward flow of extraembryonic fluid in mice lacking KIF3B motor protein. *Cell* **95**, 829-837. doi:10.1016/S0092-8674(00)81705-5

Nonaka, S., Yoshiba, S., Watanabe, D., Ikeuchi, S., Goto, T., Marshall, W. F. and Hamada, H. (2005). De novo formation of left-right asymmetry by posterior tilt of nodal cilia. *PLoS Biol.* **3**, e268. doi:10.1371/journal.pbio.0030268

Okada, Y., Takeda, S., Tanaka, Y., Belmonte, J.-C. I. and Hirokawa, N. (2005). Mechanism of nodal flow: a conserved symmetry breaking event in left-right axis determination. *Cell* **121**, 633-644. doi:10.1016/j.cell.2005.04.008

Pasapera, A. M., Plotnikov, S. V., Fischer, R. S., Case, L. B., Egelhoff, T. T. and Waterman, C. M. (2015). Rac1-dependent phosphorylation and focal adhesion recruitment of myosin IIA regulates migration and mechanosensing. *Curr. Biol.* **25**, 175-186. doi:10.1016/j.cub.2014.11.043

Shi, D., Usami, F., Komatsu, K., Oka, S., Abe, T., Uemura, T. and Fujimori, T. (2016). Dynamics of planar cell polarity protein Vangl2 in the mouse oviduct epithelium. *Mech. Dev.* **141**, 78-89. doi:10.1016/j.mod.2016.05.002

Shibata, K., Sakai, H., Huang, Q., Kamata, H., Chiba, Y., Misawa, M., Ikebe, R. and Ikebe, M. (2015). Rac1 regulates myosin II phosphorylation through regulation of myosin light chain phosphatase. *J. Cell. Physiol.* **230**, 1352-1364. doi:10.1002/jcp.24878

Shindo, A. and Wallingford, J. B. (2014). PCP and septins compartmentalize cortical actomyosin to direct collective cell movement. *Science* **343**, 649-652. doi:10.1126/science.1243126

Shinohara, K., Kawasumi, A., Takamatsu, A., Yoshiba, S., Botilde, Y., Motoyama, N., Reith, W., Durand, B., Shiratori, H. and Hamada, H. (2012). Two rotating cilia in the node cavity are sufficient to break left-right symmetry in the mouse embryo. *Nat. Commun.* **3**, 622. doi:10.1038/ncomms1624

Song, H., Hu, J., Chen, W., Elliott, G., Andre, P., Gao, B. and Yang, Y. (2010). Planar cell polarity breaks bilateral symmetry by controlling ciliary positioning. *Nature* **466**, 378-382. doi:10.1038/nature09129

Tanimoto, H., Kimura, A. and Minc, N. (2016). Shape-motion relationships of centering microtubule asters. *J. Cell Biol.* **212**, 777-787. doi:10.1083/jcb.201510064

Tanimoto, H., Salle, J., Dodin, L. and Minc, N. (2018). Physical forces determining the persistency and centering precision of microtubule asters. *Nat. Phys.* **14**, 848-854. doi:10.1038/s41567-018-0154-4

Toya, M., Kobayashi, S., Kawasaki, M., Shioi, G., Kaneko, M., Ishiuchi, T., Misaki, K., Meng, W. and Takeichi, M. (2016). CAMSAP3 orients the apical-to-basal polarity of microtubule arrays in epithelial cells. *Proc. Natl. Acad. Sci. USA* **113**, 332-337. doi:10.1073/pnas.1520638113

Tsukasaki, Y., Miyazaki, N., Matsumoto, A., Nagae, S., Yonemura, S., Tanoue, T., Iwasaki, K. and Takeichi, M. (2014). Giant cadherins Fat and Dachsous self-bend to organize properly spaced intercellular junctions. *Proc. Natl. Acad. Sci. USA* **111**, 16011-16016. doi:10.1073/pnas.1418990111

Wallingford, J. B. and Mitchell, B. (2011). Strange as it may seem: the many links between Wnt signaling, planar cell polarity, and cilia. *Genes Dev.* **25**, 201-213. doi:10.1101/gad.2008011

Zhu, J., Burakov, A., Rodionov, V. and Mogilner, A. (2010). Finding the cell center by a balance of dynein and myosin pulling and microtubule pushing: a computational study. *Mol. Biol. Cell* **21**, 4418-4427. doi:10.1091/mbc.e10-07-0627

DEVELOPMENT